Batteries & Supercaps

Research Article
doi.org/10.1002/batt.202400223

Chemistry
Europe
European Chemical
Societies Publishing

www.batteries-supercaps.org

Thermally Controlled Synthesis of $Cr_2(NCN)_3$/CrN Heterostructured Composite Anodes for High-Performance Li-Ion Batteries

Hanlou Li,[a, b] Penghui Guo,[a, b] Jing Wang,*[a, b] Silong Zhao,[a, b] Mohan Yang,[a, b] Xingxing Liu,[b] Lian Wang,[b] Meng Wang,[b] Feng Wu,[a, b] and Guoqiang Tan*[a, b]

$Cr_2(NCN)_3$ features high specific capacity and fast electrical conductivity, making it a promising anode candidate for Li-ion batteries. However, inherent chemical and structural metastability severely restrict its capacity output and cycle life, resulting in unsatisfactory battery performance. Here we use its thermal instability characteristic and propose a thermal controlled structural coordination strategy to in-situ construct a $Cr_2(NCN)_3$/CrN heterostructure. Systematic studies reveal the thermodynamic structural evolution of $Cr_2(NCN)_3$ under precise temperature regulation, as well as the essential relevancy between electrochemical properties and crystalline structures. An optimal $Cr_2(NCN)_3$/CrN heterostructural composite obtained at 690 °C features uniform two-phase recombination with abundant grain boundaries enables promising electrochemical performance, exhibiting a high reversible discharge capacity (760 mAh g^{-1}) and a good cycle performance (75 % retention after 100 cycles). It is worth noting that the above performance is significantly improved over unmodified pure transition metal carbodiimides or metal nitride anodes. This study provides a simple and universal structural regulation strategy for transition metal carbodiimides that utilizes their thermal sensitivity to synchronously construct synergistic transition metal carbodiimides/ transition metal nitrides heterostructures, promoting their potential applications in Li-ion batteries.

Introduction

Li-ion batteries (LIBs) have been widely used in various fields of electrics and electronics, especially in electric transport devices. Unfortunately, the range anxiety hinders their practical applications.[1,2] In general, improving the energy density of LIBs is considered as the most straightforward way to address this issue.[3] However, the current widely used commercial graphite anodes have low theoretical specific capacity (372 mAh g^{-1}) that can not satisfy the needs of developing high-energy LIBs.[4] Therefore, it is of great significance to pursue potential anode candidates that can deliver higher specific capacities.

Recently, transition metal carbodiimides (TMCs) have been reported as promising anode candidates for LIBs due to their high specific capacities.[5] With a general formula $M_x(NCN)_y$ (M=Fe, Mn, Zn, Ag, etc.), TMCs take $(NCN)^{2-}$ as the anion that is similar to O^{2-} and S^{2-} in terms of electronegativity and electrical charge (-2). Thus, TMCs exhibit similar coordination numbers and physicochemical properties with transition metal oxides and chalcogenides.[6] Differently, the unique quasi-linear anion $(NCN)^{2-}$ endows TMCs with spacious crystalline structures for Li-ion migration, which alleviates volume expansion and improves the stability of electrodes.[7] Meanwhile, $(NCN)^{2-}$ could adopt a special structural transformation between $(N≡C=N)^{2-}$ and $(N-C≡N)^{2-}$ to enhance electronic transport.[8] Therefore, typical TMCs such as MnNCN and FeNCN have exhibited outstanding electrochemical performance in LIBs.[9,10] Unfortunately, $(NCN)^{2-}$ as an organic group will decrease thermal stability of TMCs, which restricts traditional modification strategies associated with high-temperature treatments.[11–15] However, some studies took advantage of their thermal sensitivity to force TMCs' deliberate decomposition for the structural design or the synthesis of carbon materials with controlled nitrogen content.[16,17] According to previous reports, TMCs could convert to transition metal nitrides (TMNs) at higher sintering temperatures. Likewise, TMNs are promising candidates for LIBs anode owing to their high theoretical capacities, good chemical stability, and low electrical resistance.[18,19] Nevertheless, they always suffer from severe volume change and large polarization issues,[20–22] largely limiting practical applications. Therefore, developing $Cr_2(NCN)_3$/CrN composites via adjusting the sintering temperature might be an advisable strategy to improve the electrochemical performance.

Herein, we present a facile modification strategy to obtain TMCs/TMNs composites by taking advantage of thermal metastability of TMCs. In this work, $Cr_2(NCN)_3$ is taken as an example and the $Cr_2(NCN)_3$/CrN composites were successfully synthesized by adjusting the sintering temperature. Comprehensive characterizations were carried out to investigate their structural and chemical components. As a result, the $Cr_2(NCN)_3$/CrN composite synthesized at 690 °C exhibits the most enhanced

[a]   H. Li, P. Guo, Dr. J. Wang, S. Zhao, M. Yang, Prof. F. Wu, Prof. G. Tan
      School of Materials Science & Engineering
      Beijing Institute of Technology
      Beijing, 100081, China
      E-mail: wangjingbit98@bit.edu.cn
              tan123@bit.edu.cn
[b]   H. Li, P. Guo, Dr. J. Wang, S. Zhao, M. Yang, X. Liu, Dr. L. Wang, Dr. M. Wang,
      Prof. F. Wu, Prof. G. Tan
      Chongqing Innovation Center
      Beijing Institute of Technology
      Chongqing, 401120, China

Batteries & Supercaps

Research Article
doi.org/10.1002/batt.202400223

Chemistry
Europe

European Chemical
Societies Publishing

ionic and electronic transport features. Also, it shows superior cycle and rate performance, which can deliver 525.3 mAh g^{-1} after 100 cycles under 200 mA g^{-1} and maintain 219.4 mAh g^{-1} at 2 A g^{-1}. More importantly, this work proposes a universal modification strategy for TMCs that could be promoted to other TMCs to enhance their electrochemical performance in LIBs.

Results and Discussion

After obtaining all samples via the solid phase sintering method, we first evaluated their crystal structures by using X-ray diffraction (XRD) and Raman spectroscopy measurements. In Figure 1a, CrNCN-670 and CrNCN-690 display two sets of characteristic diffraction peaks, which can be indexed to Cr$_2$(NCN)$_3$ (CSD No. 421391) and CrN (CSD No.37412) respectively. Comparing the patterns of CrNCN-670 and CrNCN-690, the intensity of the Cr$_2$(NCN)$_3$ peaks decreases whereas the intensity of CrN peaks increases, implying that Cr$_2$(NCN)$_3$ partially converts into CrN with the temperature rises. By comparison, the pattern of CrNCN-710 only shows the diffraction peaks of CrN, indicating that Cr$_2$(NCN)$_3$ is fully converted to CrN. We then employed Raman spectroscopy to further identify their crystalline structures. In Figure 1b, both CrNCN-670 and CrNCN-690 show four Raman bands: two bands at 1375 and 1570 cm^{-1} are attributed to D and G bands[23] of N-doped carbon derived from melamine pyrolysis;[10,24] one band at 1470 cm^{-1} is assigned to the symmetrical vibration (v^s) of (N=C=N)$^{2-}$ while the other band at 1280 cm^{-1} is related to the bending mode (2δ) of (N=C=N)$^{2-}$ in Cr$_2$(NCN)$_3$.[25] As increasing temperature, D and G bands gradually decrease, indicating the further structural degradation of N-doped carbon. Similarly, the

v^s band gets weakened and finally disappears in the CrNCN-710, confirming the completely conversion of Cr$_2$(NCN)$_3$ to CrN. In short, the crystal structural evolution of samples has been confirmed. In addition, a preliminary comparison was made between the contents of Cr$_2$(NCN)$_3$ and CrN phases in three samples, which is consistent with the subsequent chemical structure analysis.

Therefore, we further characterized the chemical structures of all samples via Fourier transform infrared (FT-IR) and X-ray photoelectron spectroscopy (XPS) spectroscopy tests. In Figure 1c, CrNCN-670 displays a sharp band near 2000 cm^{-1} and a broad one from 2020 to 2178 cm^{-1}, which are attributed to the asymmetrical stretching vibration (v^{as}) of (N=C=N)$^{2-}$ in Cr$_2$(NCN)$_3$. Besides, a weak but wide band from 1139 to 1670 cm^{-1} represents the v^{as} of (N≡C−N)$^{2-}$ and two sharp bands at 694 and 634 cm^{-1} are due to the bending vibration (δ) of (N=C=N)$^{2-}$.[26] Likewise, CrNCN-690 also exhibits the same bands whereas the transmittance is higher, suggesting the lower content of (NCN)$^{2-}$. As expected, all bands mentioned above disappear in CrNCN-710 due to the thorough decomposition of Cr$_2$(NCN)$_3$. In addition, we employed XPS spectroscopy to further investigate their chemical structures. In C 1s spectra (Figure 1d), all curves consist of six bands where the strongest at 284.6 eV represents the graphitic carbon.[27] Other bands at 283.8, 286.1, 286.7, 288.1, and 288.8 eV are assigned to C−Cr, C−N, C=N, C−O, and C=O bonds respectively.[28–30] Among them, the band standing for the C=N bond gradually weakens from CrNCN-670 to CrNCN-710, indicating the decomposition of Cr$_2$(NCN)$_3$. In N 1s spectra (Figure 1e), all curves show four bands where the bands around 395.7 and 397.1 eV[31,32] represent the interaction between Cr and N within CrN and Cr$_2$(NCN)$_3$ respectively. In CrNCN-710, the intensity of the band
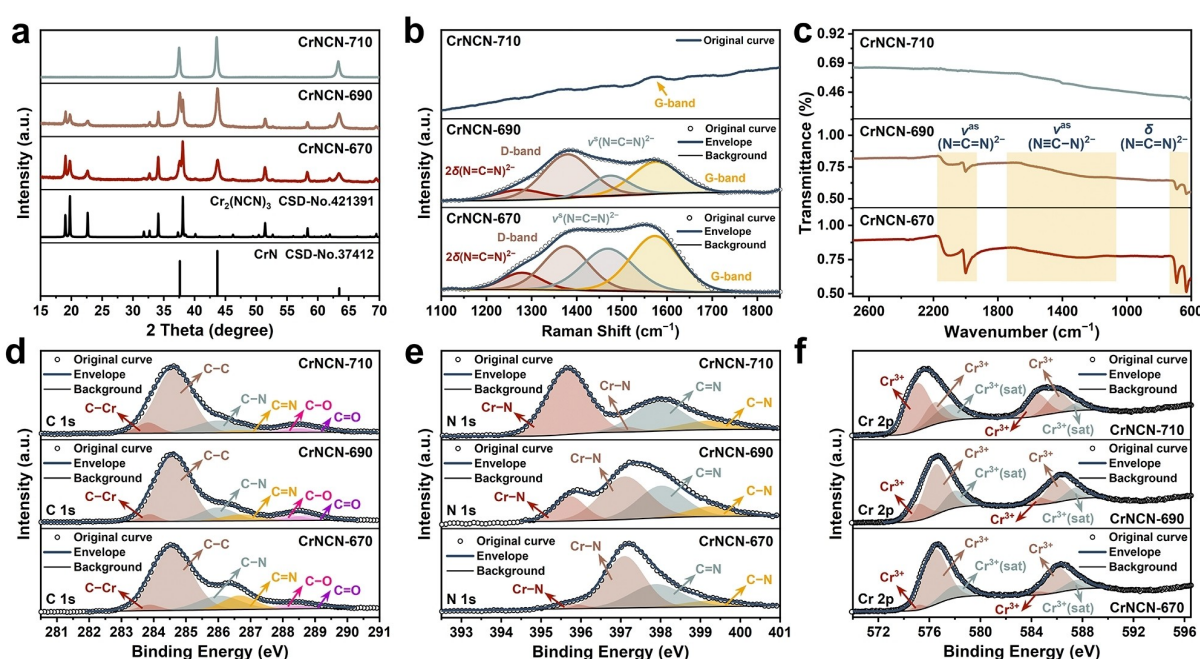

Figure 1. (a) XRD patterns, (b) Raman spectra, (c) FT-IR spectra of samples: CrNCN-670, CrNCN-690, and CrNCN-710. (d–f) XPS spectra of (d) C 1s, (e) N 1 s, and (f) Cr 2p of CrNCN-670, CrNCN-690, and CrNCN-710.

Batteries & Supercaps

Research Article
doi.org/10.1002/batt.202400223

Chemistry Europe
European Chemical
Societies Publishing

at 395.7 eV is the highest while the intensity of the other at 397.1 eV is the lowest compared to others, confirming that it has the highest CrN phase content and the lowest one of $Cr_2(NCN)_3$. In Cr 2p spectra (Figure 1f), two bands near 576 and 586 eV are derived from Cr $2p_{1/2}$ and $2p_{3/2}$. Notably, the intensity of the peaks at 573.5 and 584.3 eV increases gradually whereas the peak at 576.3 eV weakens from CrNCN-670 to CrNCN-710, probably due to the increase of CrN phase content and the decreasing one of $Cr_2(NCN)_3$. In brief, these characterizations prove that $Cr_2(NCN)_3$/CrN heterostructural composites with different $Cr_2(NCN)_3$ phase content could be in-situ obtained by adjusting the sintering temperature. Meanwhile, these samples might display distinct microstructures due to the degradation of $Cr_2(NCN)_3$ and the formation of CrN.

We then investigated their morphologies and microstructures by using scanning electron microscopy (SEM) and transmission electron microscopy (TEM) measurements. In Figure 2a, CrNCN-670 shows a lamellar structure that matches the typical morphology of $Cr_2(NCN)_3$.[33] Notably, there are some tiny nanoparticles around the sheet-like $Cr_2(NCN)_3$, probably due to the presence of CrN. In Figure 2b, CrNCN-690 shows a distinctive morphology in which the sheet-like $Cr_2(NCN)_3$ becomes smaller while the surrounding particles increase significantly. This finding indicates that $Cr_2(NCN)_3$ may decompose and produce more CrN particles as the temperature increases from 670 to 690 °C. In Figure 2c, CrNCN-710 displays

nanoparticles with diameters from about 100 to 200 nm. As expected, no lamellar structure was observed, suggesting the completely conversion from $Cr_2(NCN)_3$ to CrN. Notably, all these $Cr_2(NCN)_3$ and/or CrN particles are grown onto a N-doped carbon substrate, which is marked by orange dashed lines in Figures 2a–c. According to previous reports,[10,32] N-doped carbon substrate is derived from the thermal polymerization of the melamine since it is excess in the reactants. More importantly, this finding rationalizes the presence of D and G bands in Raman spectra and the presence of C–N and C=N bonds in N 1s XPS spectra (Figures 1b and 1e). We then performed TEM (Figures 2d–f) to investigate their micro-structural difference. Considering the existence of N-doped carbon, we selected the surface $Cr_2(NCN)_3$ and/or CrN without the N-doped carbon for TEM tests. As a result, the diffraction rings corresponding to $Cr_2(NCN)_3$ planes (red circles) gradually decrease while rings attributing to CrN planes (orange circles) become increasingly clear in selected area electron diffraction (SAED) patterns (insertion in Figures 2d–f). Moreover, the high-resolution TEM (HRTEM) image of CrNCN-670 (Figure 2g) demonstrates the co-existence of $Cr_2(NCN)_3$ and CrN, as the lattice stripes corresponding to $Cr_2(NCN)_3$ (116) and CrN (220) planes are identified. Note that the strips of $Cr_2(NCN)_3$ are dominant but the grain boundaries between $Cr_2(NCN)_3$/CrN two-phase are not distinctive. In contrast, CrNCN-690 (Figure 2h) displays uniform two-phase recombination with clear
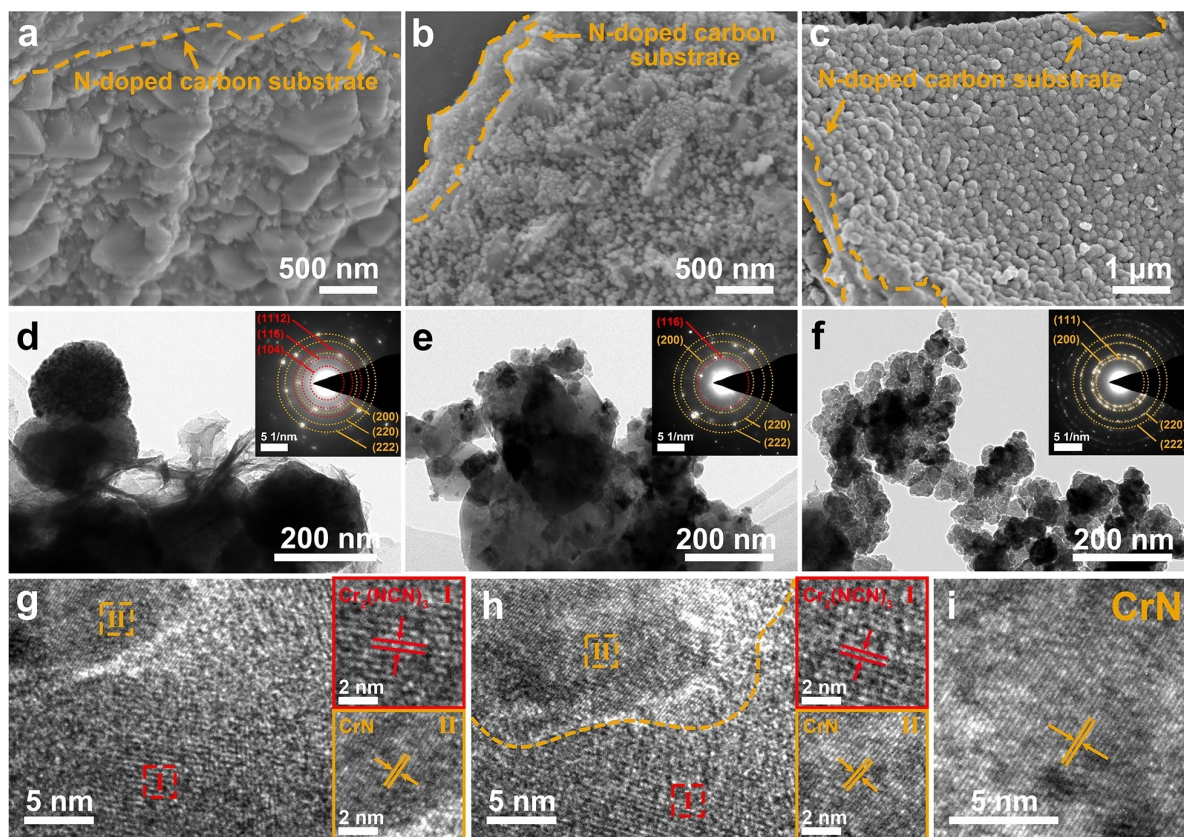

Figure 2. (a–c) SEM images of (a) CrNCN-670, (b) CrNCN-690, and (c) CrNCN-710. (d–f) TEM images and SAED patterns of (d) CrNCN-670, (e) CrNCN-690, and (f) CrNCN-710. (g–i) HRTEM images of (g) CrNCN-670, (h) CrNCN-690, and (i) CrNCN-710.

Batteries & Supercaps

Research Article
doi.org/10.1002/batt.202400223

Chemistry Europe
European Chemical
Societies Publishing

grain boundaries. The stripes of CrN get well-defined since the crystallinity of CrN is increased. As expected, CrNCN-710 has clear strips of CrN but no $Cr_2(NCN)_3$ (Figure 2i). Briefly, SEM and TEM measurements disclose the morphological difference between three samples, while HRTEM images further confirm the clear grain boundaries of $Cr_2(NCN)_3$/CrN heterostructure within CrNCN-690. We then performed thermogravimetry analysis (TGA) to determine the $Cr_2(NCN)_3$ content of three samples. In Figure 3a, CrNCN-670 and CrNCN-690 show similar TGA profiles consisting of four stages: below 626 °C (stage 1), between 626 and 875 °C (stage 2), between 875 and 1018 °C (stage 3) and above 1018 °C (stage 4). Differently, CrNCN-710 exhibits three stages without stage 1. Based on the above XRD, Raman, FT-IR, and XPS results, stage 1 is believed to be attributed to the decomposition from $Cr_2(NCN)_3$ to CrN, stage 2 corresponds to the conversion of CrN to Cr_2N, and stage 3 is the further conversion of Cr_2N to Cr.[34,35] Figure 3b compares the detail weight loss of these four stages for three samples. Combined with the analysis of SEM and TEM, we proposed a schematic to demonstrate the structural evolution from CrNCN-670 to CrNCN-710 (Figure 3c). When at 670 °C, $Cr_2(NCN)_3$ begins to pyrolyze, and some edge regions of the lamellar $Cr_2(NCN)_3$ are transformed into CrN. In this case, CrNCN-670 maintains the microspherical shape and the bulk lamellar $Cr_2(NCN)_3$ structure with a small amount of CrN nanocrystallines. At 690 °C, the transformation from $Cr_2(NCN)_3$ to CrN is largely improved, and the CrN grains grow up to form more nanoparticles, which are attached to $Cr_2(NCN)_3$ microspheres, so CrNCN-690 shows significant two-phase recombination with rich grain boundaries. At 710 °C, $Cr_2(NCN)_3$ microspheres are completely pyrolyzed to CrN nanoparticles, so CrNCN-710 shows the pure CrN crystalline feature. That is, $Cr_2(NCN)_3$ converts to CrN spontaneously as increasing the sintering temperature. The above finding confirms that the $Cr_2(NCN)_3$/CrN heterostructures with different CrN contents can be in-situ synthesized by adjusting the sintering

temperature. Preciously, at 690 °C, the obtained CrNCN-690 features uniform two-phase recombination with rich grain boundaries, may be beneficial to electrical and electrochemical properties.

To explore the electrical properties of CrNCN-670, CrNCN-690, and CrNCN-710, we employed cyclic voltammetry (CV) and electrochemical impedance spectroscopy (EIS) tests to evaluate Li-ion diffusion behaviors and electron transport features in these three electrodes. Figures 4a-c compare CV profiles performed at a scan rate of 0.1 mV s^{-1}. From CrNCN-670 to CrNCN-690 (Figures 4a and 4b), the sharp peak around 0.5 V in their initial cycles gets weakened gradually, suggesting the Li-ion interaction into $Cr_2(NCN)_3$/CrN heterostructural composites as well as the decrease tendency of the $Cr_2(NCN)_3$ content. In Figure 4c, a tiny peak at 0.5 V at the first cycle represents the reaction between CrN and Li-ion. Furthermore, Figures 4d–f compare CV profiles of three samples under various scan rates, and all results were collected from the second cycle. In Figure 4d, CrNCN-670 shows two couples of peaks A_1/A_2 and B_1/B_2 located at 0.01/0.95 V and 0.55/1.58 V respectively. Likewise, CrNCN-690 (Figure 4e) displays the same two peaks while they are around 0.01/1.09 V and 0.69/1.65 V. Normally, peaks A_1 and A_2 stand for the intercalation and deintercalation of Li-ions in/out the carbon matrix and the formation of solid electrolyte interphase (SEI).[36,37] In contrast, peaks B_1 and B_2 are attributed to multiple reactions between Li-ion and $Cr_2(NCN)_3$/CrN composites. In contrast, CrNCN-710 (Figure 4f) exhibits three peak couples A_1/A_2, B_{N1}/B_{N2}, and C_{N1}/C_{N2} located at 0.01/1.06 V, 0.43/1.83 V, and 1.37/2.73 V, where couples B_N and C_N are attributed to the reactions of Li-ions with CrN.[38] Impressively, the gap between peaks B_1 and B_2 in CrNCN-670 and CrNCN-690 is 1.03 and 0.96 V, dramatically lower than the gap between peaks B_{N1} and B_{N2} in CrNCN-710 (1.4 V). This finding confirms that the CrN has the severe polarization, while combining the $Cr_2(NCN)_3$ this issue could be alleviated, especially for the $Cr_2(NCN)_3$/CrN
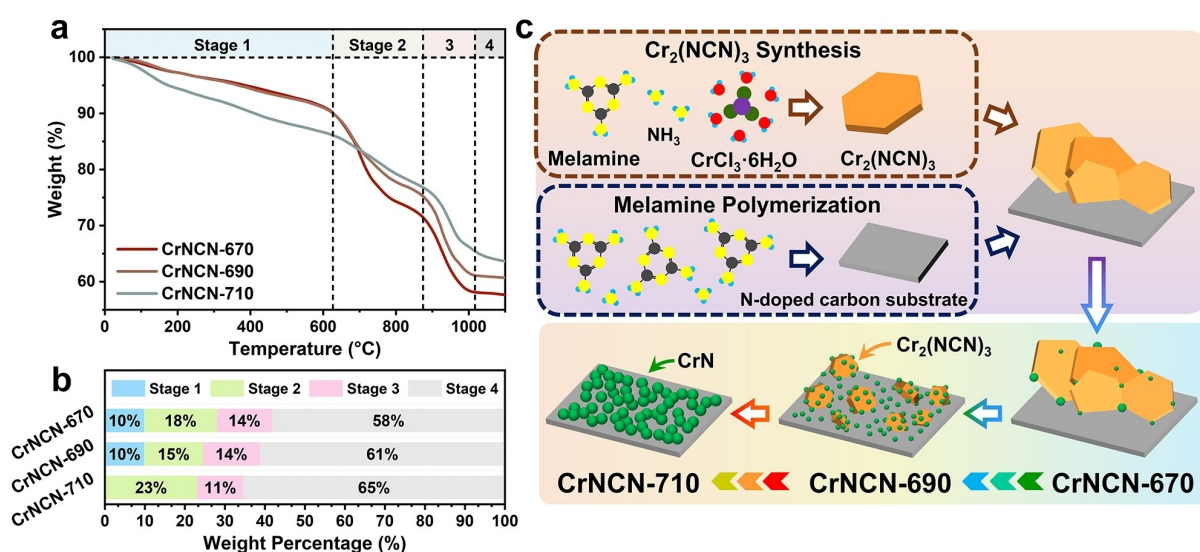

Figure 3. (a) TGA profiles of CrNCN-670, CrNCN-690, and CrNCN-710. (b) Weight loss at different stages. (c) Schematic diagram of structural evolution of $Cr_2(NCN)_3$ under sintering.
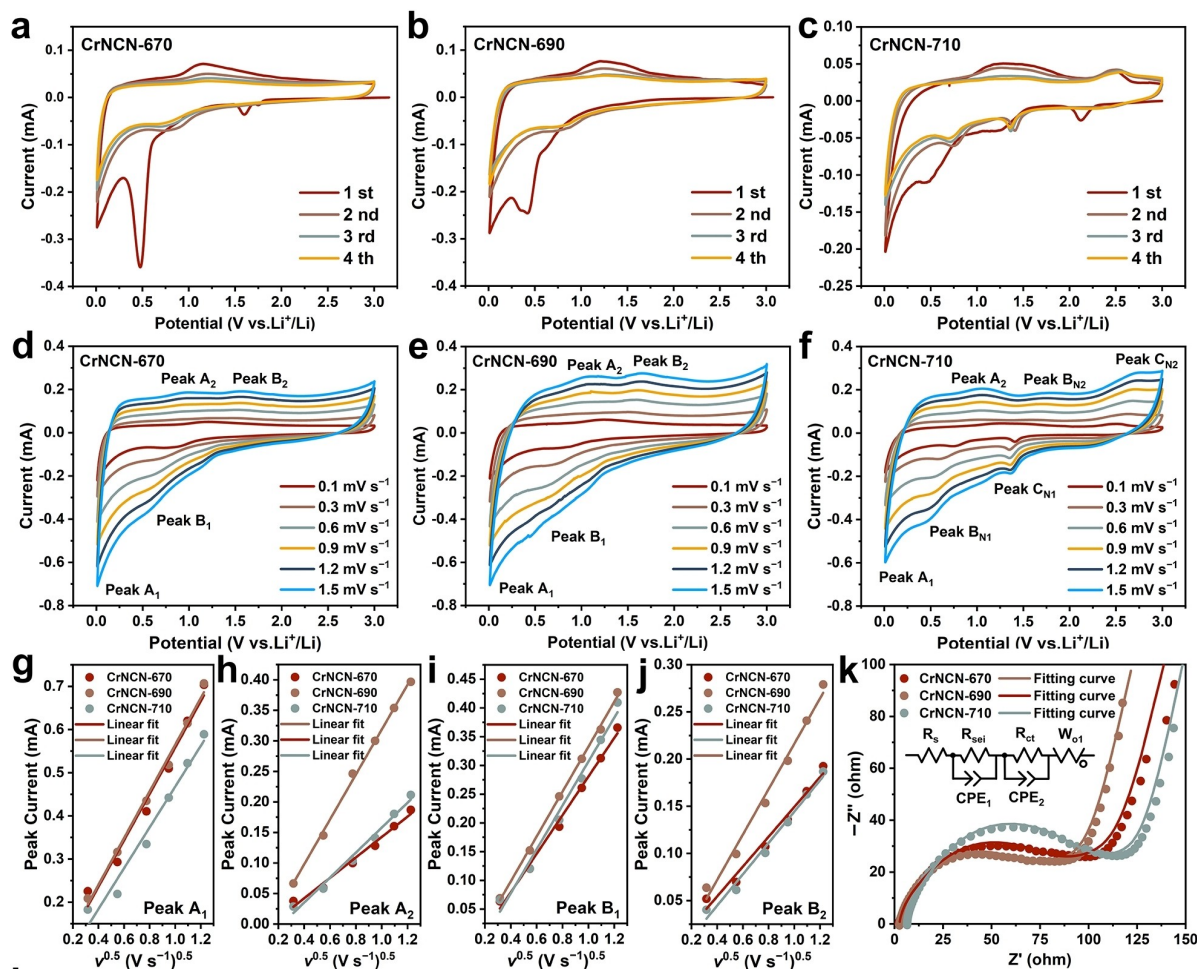
Batteries & Supercaps

Research Article
doi.org/10.1002/batt.202400223

Chemistry
Europe

European Chemical
Societies Publishing

Figure 4. (a–c) CV curves of (a) CrNCN-670, (b) CrNCN-690, and (c) CrNCN-710 at 0.1 mV s^{-1}. (d–f) CV curves of (d) CrNCN-670, (e) CrNCN-690, and (f) CrNCN-710 at different scan rates. (g–j) CV peak current values of A$_1$, A$_2$, B$_1$, and B$_2$ for CrNCN-670, CrNCN-690, and CrNCN-710 versus the square root of scan rates. (k) EIS Nyquist plots of CrNCN-670, CrNCN-690, and CrNCN-710 before cycling tests.

heterostructure. Additionally, based on CV profiles we investigated the Li-ion diffusion behaviors in electrodes using the Randles-Sevcik equation:[39]

$$I_p = (2.69 \times 10^5) \; n^{1.5} A D^{0.5} C \nu^{0.5} \tag{1}$$

where I_p, n, A, D, C, and ν represent peak current, number of electrons, electrode area, Li-ion diffusion coefficient, Li-ion concentration, and scan rate, respectively. As shown in Figure 4g, CrNCN-670 and CrNCN-690 exhibit similar slopes at peak A$_1$ which are higher than that of CrNCN-710. Besides, CrNCN-690 shows the highest slope at peak A$_2$ (Figure 4h). These findings indicate that the carbon matrix of CrNCN-690 exhibits the fastest Li-ion diffusion behavior compared to others due to the structural difference in their carbon matrices shown in Raman spectra. Furthermore, CrNCN-690 also shows the highest slopes at peaks B$_1$ and B$_2$ (Figures 4i–j), confirming the enhanced Li-ion diffusion behavior.[40]

We then employed EIS tests to evaluate their electrical conduction features. Figure 4k compares Nyquist plots of three electrodes before cycling tests and all curves consist of a semicircle in high-frequency region and a sloped line in low-frequency area. Comparatively, CrNCN-690 shows the smallest semicircle while CrNCN-710 has the biggest one. According to the equivalent circuit (insertion in Figure 4k), the resistance of solid electrolyte interphase (R$_{sei}$) and the resistance of charge-transfer (R$_{ct}$) of all three plots were fitted. As expected, CrNCN-690 shows the lowest R$_{sei}$ (3.37 Ω) and R$_{ct}$ (59.56 Ω) compared to CrNCN-670 (7.11 and 67.79 Ω) and CrNCN-710 (6.89 and 100.50 Ω). This finding indicates the best electrode dynamics of CrNCN-690 among three electrodes. As described above, with increasing the sintering temperature from 670 °C to 690 °C, more Cr$_2$(NCN)$_3$ are pyrolyzed and transformed into CrN to forming two-phase grain boundaries. These abundant grain boundaries are always beneficial for the electron and ion transport, and also provide high reaction activity, which are believed to be attributing to high electrochemical capacity and rate capability. In short, CV and EIS measurements demonstrate the fastest Li-ion and electron transport behavior of the CrNCN-690, which may contribute to excellent electrochemical properties.

Batteries & Supercaps

Research Article
doi.org/10.1002/batt.202400223

Chemistry Europe
European Chemical
Societies Publishing

To evaluate their electrochemical performance in LIBs, we first carried out galvanostatic charge-discharge measurements to evaluate their lithium storage capacities and cycle stability. Figures 5a–c compare their voltage profiles at primary three cycles. CrNCN-670 (Figure 5a) shows a clear plateau around 0.5 V, which is consistent with its CV curves. As expected, this plateau is weaken in CrNCN-690 (Figure 5b) and disappears finally in CrNCN-710 (Figure 5c). Moreover, CrNCN-690 exhibits the lowest capacity decay between the second and the third cycles, which indicates the possible higher stability in the cycling test. Thus, we present Figures 5d–f to compare their voltage profiles after different cycles. At all the selected cycles, CrNCN-690 delivers the highest capacities while CrNCN-710

displays the lowest capacities. Besides, CrNCN-690 also displays the best cycling stability. In Figure 5g, it can maintain a high capacity of 525.3 mAh g^{-1} with a high retention of 75% after 100 cycles at 200 mA g^{-1}. Comparatively, CrNCN-670 delivers a low capacity of 374.6 mAh g^{-1} and CrNCN-710 just delivers a lower capacity of 238.3 mAh g^{-1}. Except for the best Li-ion storage capacity and cycling stability, CrNCN-690 also has the best rate performance. In Figure 5h, CrNCN-690 displays stable cycle performance at each current density and can deliver 219.4 mAh g^{-1} at 2 A g^{-1} whereas CrNCN-670 and CrNCN-710 only deliver 106.0 and 83.5 mAh g^{-1}. In addition, the capacity of CrNCN-690 can recover when the current density is resumed to 0.1 A g^{-1}. To further understand the cycle performance, we
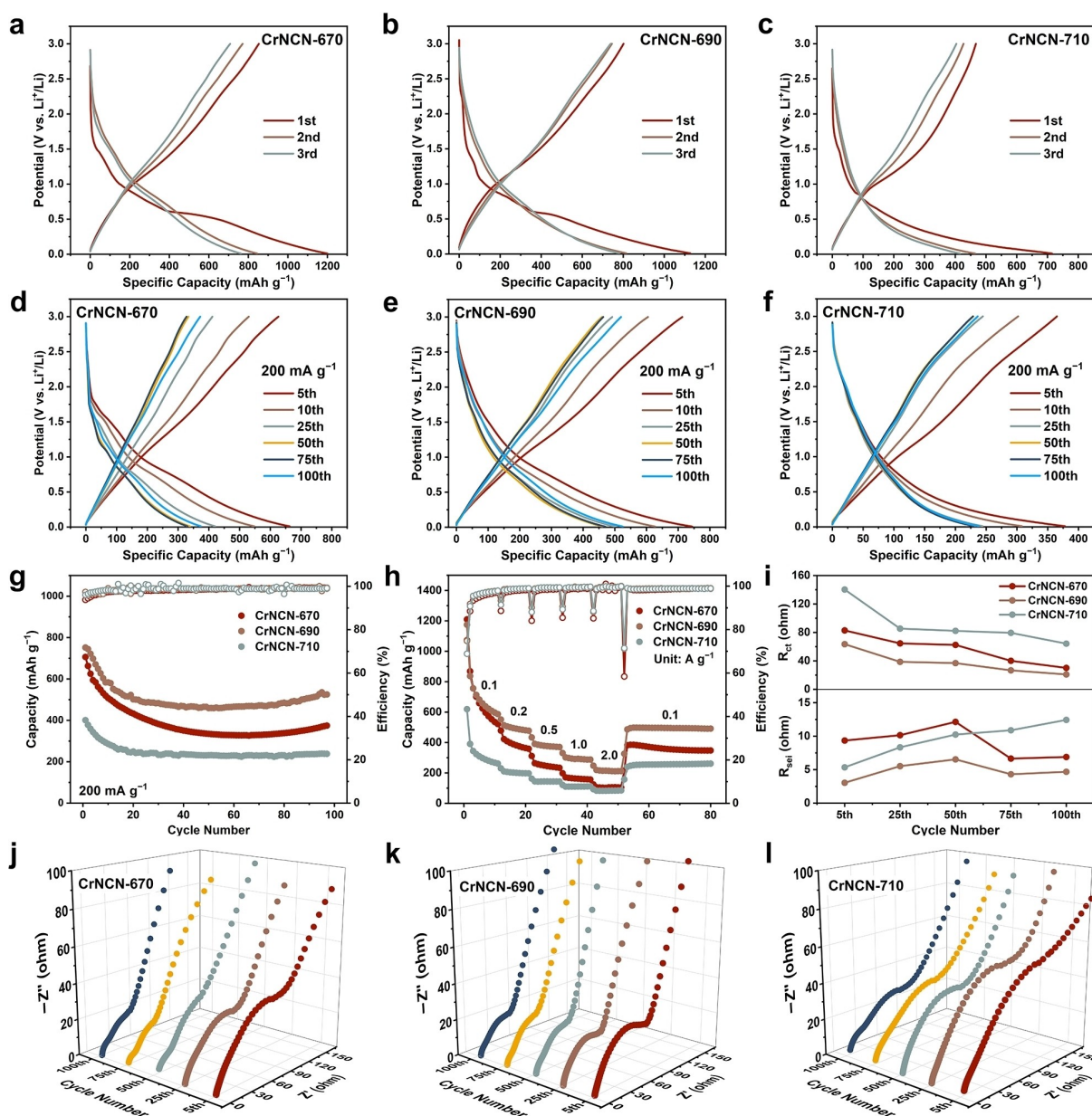

Figure 5. Electrochemical performance for Li-ion storage. (a–c) Voltage profiles of (a) CrNCN-670, (b) CrNCN-690, and (c) CrNCN-710 at primary three cycles at 0.2 A g^{-1}. (d–f) Voltage profiles of (d) CrNCN-670, (e) CrNCN-690, and (f) CrNCN-710 at different cycles. (g) Cycling performance of CrNCN-670, CrNCN-690, and CrNCN-710 at 0.2 A g^{-1}. (h) Rate performance of CrNCN-670, CrNCN-690, and CrNCN-710 at different current densities. (i) Plots of R_{ct} and R_{sei} against different cycles for CrNCN-670, CrNCN-690, and CrNCN-710. (j–l) Nyquist plots of (j) CrNCN-670, (k) CrNCN-690, and (l) CrNCN-710 electrodes after different cycles.

Batteries & Supercaps

Research Article
doi.org/10.1002/batt.202400223

Chemistry Europe
European Chemical
Societies Publishing

performed EIS tests at different cycle numbers. Figure 5i compares the R_{ct} and R_{sei} of three electrodes during cycling and all Nyquist plots are shown in Figures 5j–l. As shown in Figure 5i, three electrodes show the similar impedance trends as the cycle increases. Among them, CrNCN-690 exhibits the lowest R_{sei} and R_{ct} values with best stability compared to CrNCN-670 and CrNCN-710 during the whole cycling, confirming the above best cell performance, including the highest reversible capacity and best cycle performance. Generally, R_{sei} indicates the resistance of Li-ions across the SEI layer[41] and R_{ct} is the charge-transfer resistance to identify electrode dynamics.[42] As a result, the most stable R_{sei} of CrNCN-690 suggests its stable surface SEI layer, and the lowest R_{ct} of CrNCN-690 demonstrates excellent electrode dynamics, both of them are beneficial for Li-ion intercalation/deintercalation to/out the CrNCN-690 electrode. That is, CrNCN-690 exhibits the fastest Li-ion approaching across the electrode surface and also the most efficient charge-transfer processes, thus delivering the highest reversible capacities and the best cycle performance.[43]

Based on the above analysis, among three electrodes, CrNCN-690 has the most uniform $Cr_2(NCN)_3$/CrN two-phase combination with abundant grain boundaries, it exhibits the best electrochemical performance; CrNCN-670 containing the main $Cr_2(NCN)_3$ structure with a small amount of grain boundaries delivers a high initial capacity but with poor cycle stability; CrNCN-710 featuring the pure CrN crystalline suffers from sluggish electrode dynamics and severe volume change, resulting in poor electrochemical performance. Overall, the enhanced electrochemical performance of CrNCN-690 could be mainly attributed to uniform two-phase recombination with abundant grain boundaries, which bears a significant synergistic effect.[44] Notably, similar to transition metal oxides and chalcogenides, both $Cr_2(NCN)_3$ and CrN suffer from the low potential, making them not ideal as either cathodes or anodes in LIBs. To tackle this problem, the advantages of $Cr_2(NCN)_3$/CrN heterostructural electrode can be maximized by matching high-potential cathodes and combining prelithiation technique to build a full-cell configuration. Generally, the prelithiation design for $Cr_2(NCN)_3$/CrN anode is used to address the impact of the initial capacity loss, which has been widely used, particularly for alloy and conversion anode materials. The $Cr_2(NCN)_3$/CrN heterostructural materials developed here show promise for use in advanced LIBs.

Conclusions

In summary, $Cr_2(NCN)_3$/CrN heterostructural composites were in-situ synthesized via a simple solid-phase sintering method by adjusting sintering temperatures precisely. Systematic studies determined that the optimized CrNCN-690 had a lower $Cr_2(NCN)_3$ content but a higher CrN content in comparison to CrNCN-670. Notably, the CrNCN-690 exhibited uniform two-phase recombination with abundant grain boundaries that contribute to excellent electrical properties and promising electrochemical performance. Comparatively, CrNCN-690 exhibits better cell performance than either CrNCN-670 or CrNCN-710

anodes. The study provides a simple and universal structural regulation strategy for TMCs that utilizes their thermal meta-stability to synchronously construct synergistic TMCs/TMNs heterostructures, promoting their potential applications in LIBs.

Experimental Section

Material Synthesis. All materials were synthesized using a solid-phase sintering method. In detail, $CrCl_3 \cdot 6H_2O$ (1.0 g) and melamine (0.6 g) were mixed thoroughly for 15 min and then transferred into a tubular furnace. After refreshing the atmosphere with argon three times, the temperature was raised to 670, 690, 710 °C with a heating rate of 5 °C min^{-1} and maintained at 670, 690, 710 °C for 10 min. NH$_3$/Ar mixed gas (5:95 in volume) was used at a flow of 150 ml min^{-1} during sintering. All products were washed with the deionized water and dried under vacuum at 80 °C overnight.

Material Characterization. X-ray diffraction (XRD) equipped with Cu−Kα radiation and Raman spectroscopy with an excitation laser $\lambda = 532$ nm were employed to identify the crystal structures of all samples. Their chemical structures were investigated by Fourier transform infrared (FT-IR) spectroscopy and X-ray photoelectron (XPS) spectroscopy. The $Cr_2(NCN)_3$ phase content of all materials was determined by using thermogravimetry analysis (TGA) conducted under Argon flow. Microstructures and morphologies were collected via scanning electron microscope (SEM) and transmission electron microscopy (TEM).

Electrochemical Measurements. All electrodes were prepared by pasting a mixed slurry that contains active materials, acetylene black, and polyvinylidene difluoride (PVDF) with a mass ratio (7:2:1) in 1-meththyl-2-pyrrolidone (NMP) solvent onto a copper foil. The CR2032 coin cells were assembled with lithium foil as the counter electrode and polypropylene membrane (Celgard 2500) as the separator. The electrolyte is 1.0 M LiPF$_6$ dissolved into 1 L mixture of ethylene carbonate (EC), dimethyl carbonate (DMC), and diethyl carbonate (DEC) (1:1:1 in volume). The areal active mass loading of electrode is ~3 mg cm^{-2} and the added electrolyte for each cell is ~60 μL. Galvanostatic cycling tests were performed at a Land CT-2001 A instrument (Wuhan, China) between 0.01 and 3.0 V at 30 °C. Cyclic voltammetry (CV) and electrochemical impedance spectroscopy (EIS) measurements were employed at a CHI660E electrochemical workstation. The frequency range of EIS tests was from 0.1 to 100 kHz.

Conflict of Interests

The authors declare no conflict of interest.

Batteries & Supercaps

Research Article
doi.org/10.1002/batt.202400223

Chemistry Europe
European Chemical
Societies Publishing

Data Availability Statement

The data that support the findings of this study are available from the corresponding author upon reasonable request.

[1] S. L. Prasad, A. Gudipalli, *Int. Trans. Electr. Energy Syst.* **2023**, *2023*, 7246414.
[2] H. A. Bonges, A. C. Lusk, *Transport. Res. A-Pol.* **2016**, *83*, 63–73.
[3] X. Gao, H. Yang, *Energy Environ. Sci.* **2010**, *3*, 174–189.
[4] L. Zhao, B. Ding, X. Qin, Z. Wang, Y. Lv, Y. He, Q. Yang, F. Kang, *Adv. Mater.* **2022**, *34*, 2106704.
[5] A. E. Barrio, E. C. Martinez, X. Liu, R. Dronskowski, M. Armand, T. Rojo, *J. Mater. Chem. A* **2016**, *4*, 1608–1611.
[6] B. Jia, D. Sun, W. Zhao, F. Huang, *J. Energy Chem.* **2021**, *61*, 347–367.
[7] M. T. Sougrati, A. Darwiche, X. Liu, A. Mahmoud, R. P. Hermann, S. Jouen, L. Monconduit, R. Dronskowski, L. Stievano, *Angew. Chem. Int. Ed.* **2016**, *55*, 5090–5095.
[8] W. Zhao, Y. Liu, J. Liu, P. Chen, I. Chen, F. Huang, J. Lin, *J. Mater. Chem. A* **2013**, *1*, 7942–7948.
[9] C. Liu, C. Zhang, H. Fu, X. Nan, G. Cao, *Adv. Energy Mater.* **2017**, *7*, 1601127.
[10] H. Qi, Y. Hou, W. Wang, L. Tang, C. Zhang, W. Deng, Y. Cheng, J. Zhang, *Dalton Trans.* **2022**, *51*, 8223–8233.
[11] E. Zhang, Z. Luo, Y. Luo, P. Wang, S. Chen, L. Xu, X. Wang, H. Li, *Chem. Eng. J.* **2024**, *489*, 151286.
[12] M. Yuan, S. Zhang, L. Lin, Z. Sun, H. Yang, H. Li, G. Sun, C. Nan, S. Ma, *ACS Sustainable Chem. Eng.* **2019**, *7*, 17464–17473.
[13] J. Li, R. Wang, P. Guo, X. Liu, Y. Hu, Z. Xu, Y. Liu, L. Cao, J. Huang, K. Kajiyoshi, *ACS Nano* **2021**, *15*, 6410–6419.
[14] P. Guan, L. Zhou, Z. Yu, Y. Sun, Y. Liu, F. Wu, Y. Jiang, D. Chu, *J. Energy Chem.* **2020**, *43*, 220–235.
[15] J. J. Arayamparambil, M. Mann, X. Liu, M. Alfredsson, R. Dronskowski, L. Stievano, M. T. Sougrati, *ACS Omega* **2019**, *4*, 4339–4347.
[16] J. Xu, F. Xu, M. Qian, F. Xu, Z. Hong, F. Huang, *Adv. Mater.* **2017**, *29*, 1701674.
[17] J. Lin, W. Zhao, M. Qian, K. Liu, J. Xu, F. Huang, *Chem. Commun.* **2018**, *54*, 4565–4568.
[18] M. S. Balogun, Y. Huang, W. Qiu, H. Yang, H. Ji, Y. Tong, *Mater. Today* **2017**, *20*, 425–451.
[19] B. Das, M. V. Reddy, G. V. S. Rao, B. V. R. Chowdari, *RSC Adv.* **2012**, *2*, 9022–9028.
[20] Y. Yue, P. Han, S. Dong, K. Zhang, C. Zhang, C. Shang, G. Cui, *Chin. Sci. Bull.* **2012**, *57*, 4111–4118.
[21] Q. Sun, Z. Fu, *Electrochem. Solid-State Lett.* **2007**, *10*, A189–A193.
[22] Q. Sun, Z. Fu, *Electrochem. Solid-State Lett.* **2008**, *11*, A233–A237.
[23] R. Wang, J. Wang, S. Chen, W. Bao, D. Li, X. Zhang, Q. Liu, T. Song, Y. Su, G. Tan, *ACS Appl. Mater. Interfaces* **2021**, *13*, 5008–5016.
[24] B. Long, M. S. Balogun, L. Luo, Y. Luo, W. Qiu, S. Song, L. Zhang, Y. Tong, *Small* **2017**, *13*, 1702081.
[25] R. J. Müller, J. Lan, K. Lienau, R. Moré, C. A. Triana, M. Iannuzzi, G. R. Patzke, *Dalton Trans.* **2018**, *47*, 10759–10766.
[26] O. Reckeweg, A. Simon, *Z. Naturforsch.* **2003**, *58b*, 1097–1104.
[27] G. Tan, L. Chong, R. Amine, J. Lu, C. Liu, Y. Yuan, J. Wen, K. He, X. Bi, Y. Guo, H. H. Wang, R. S. Yassar, S. A. Hallaj, D. J. Miller, D. Liu, K. Amine, *Nano Lett.* **2017**, *17*, 2959–2966.
[28] J. J. Chen, N. Winograd, *Surf. Sci.* **1995**, *326*, 285–300.
[29] I. Bertoti, M. Mohai, K. Kereszturi, A. Toth, E. Kalman, *Solid State Sci.* **2009**, *11*, 1788–1792.
[30] G. M. Wilson, S. O. Saied, S. K. Field, *Thin Solid Films* **2007**, *515*, 7820–7828.
[31] A. Lippitz, Th. Hubert, *Surf. Coat. Technol.* **2005**, *200*, 250–253.
[32] P. Guo, L. Cao, R. Wang, Y. Hu, Z. Xu, J. Huang, C. Yao, L. Guo, Y. Cheng, J. Li, K. Kajiyoshi, *Adv. Funct. Mater.* **2020**, *30*, 2000208.
[33] J. J. Arayamparambil, K. Chen, A. Iadecola, M. Mann, X. Qiao, B. Fraisse, R. Dronskowski, L. Stievano, M. T. Sougrati, *Energy Technol.* **2020**, *8*, 1901260.
[34] C. Meng, J. Jiang, J. Ma, T. Zhang, W. Liu, P. Xie, H. Wang, X. Ma, X. He, *Nucl. Mater. Energy* **2023**, *37*, 101531.
[35] C. Paternoster, A. Fabrizi, R. Cecchini, M. El Mehtedi, P. Choquet, *J. Mater. Sci.* **2008**, *43*, 3377–3384.
[36] Y. Zhao, J. Wang, C. Ma, Y. Li, *Chem. Phys. Lett.* **2018**, *704*, 31–36.
[37] T. Yang, Z. Chen, H. Zhang, M. Zhang, T. Wang, *Electrochim. Acta* **2016**, *217*, 55–61.
[38] M. Idrees, S. M. Abbas, A. U. Rehman, N. Ahmad, M. W. Mushtaq, R. A. Naqvi, K. W. Nam, B. Muhammad, Z. Iqbal, *Chem. Eng. J.* **2017**, *327*, 361–370.
[39] J. Zhang, C. Sun, S. Qu, M. Qian, W. Zhan, A. Su, K. Zhang, Q. Liu, R. Shao, J. Wang, Y. Su, J. Huang, F. Wu, G. Tan, *Nano Energy* **2023**, *111*, 108401.
[40] J. Zhang, J. Wang, M. Qian, B. Zhao, R. Wang, X. Hao, X. Huang, R. Shao, Z. Xing, J. Xie, B. Xu, Y. Su, F. Wu, G. Tan, *Adv. Funct. Mater.* **2021**, *32*, 2108305.
[41] W. Choi, H. Shin, J. Kim, J. Choi, W. Yoon, *J. Electrochem. Sci. Technol.* **2020**, *11*, 1–13.
[42] M. Hasanpoor, D. Saurel, R. C. Barreno, K. Fraysse, M. Echeverría, M. Jáuregui, F. Bonilla, G. W. Greene, R. Kerr, M. Forsyth, P. C. Howlett, *ACS Appl. Mater. Interfaces* **2022**, *14*, 13196–13205.
[43] M. Cao, R. Li, F. Huang, X. Cai, M. Cui, S. Lin, J. Tian, Z. Shadike, Z. Fu, *New J. Chem.* **2023**, *47*, 12109–12116.
[44] M. Chen, Y. Lu, W. Li, P. Qi, G. Liu, S. Wang, Z. Chen, Y. Tang, *Electrochim. Acta* **2022**, *413*, 140101.